

# Stereoscopic PIV using optical flow: application to a cavity recirculation

Christelle L. Douay, Thierry M. Faure<sup>\*</sup>, François Lusseyran

*Université Pierre et Marie Curie, Sorbonne Universités,  
4 place Jussieu, 75252 Paris Cedex 05, France*

*Université Paris-Sud, 91405 Orsay Cedex, France*

*Laboratoire d'Informatique pour la Mécanique et les Sciences de l'Ingénieur,  
Unité Propre de Recherche 3251, Centre National de la Recherche Scientifique  
bât. 508 rue J. Von Neumann, B.P. 133, 91403 Orsay Cedex, France*

*\*current address: Centre de Recherche de l'Armée de l'Air (CRéA)  
Écoles d'Officiers de l'Armée de l'Air, B.A. 701, 13661 Salon-de-Provence, France*

Communicating author: Thierry M. Faure

e-mail: thierry.faure@limsi.fr

telephone: (33) 4 90 17 80 93

fax: (33) 4 90 17 81 89

## Abstract

Open cavity flows are a class of wall-bounded flows marked by a recirculation vortex, large velocity gradients and internal three-dimensional (3D) features. That complex structure results in the combination of an upper shear-layer, which can develop a Kelvin-Helmholtz-like instability interacting with walls, the flow injection inside the cavity, the recirculation vortex development, and, for some geometries and Reynolds numbers, a centrifugal Taylor-Görtler-like instability. In order to explore this flow, experimental measurements of the three components of velocity are addressed with stereoscopic two-dimensional particle image velocimetry (3C-2D PIV) using an optical flow algorithm. This technique is a valuable diagnostic tool for quantitative instantaneous description of 3D flows, as those dominated by vortex motion. PIV camera calibration is based on a pinhole model using a single target and camera focal length. The challenging issue is that the studied flow is wall-bounded, and subject to laser reflections which can alter the quality of particle images. A treatment of recorded frames is addressed to get the correct velocity field. PIV measurements are carried out in two orthogonal planes to catch the flow structure and vortex dynamics. Time development of Taylor-Görtler-like vortices is also confronted to the results obtained in previous studies.

## List of symbols

$A$	integration domain
$D$	cavity depth
$L$	cavity length
$Re$	Reynolds number
$S$	cavity span
$t$	time
$U_e$	external flow velocity
$U_i$	horizontal velocity component of camera $i$ , $i = \{1,2\}$
$U_x$	velocity component along $x$
$U_y$	velocity component along $y$
$U_z$	velocity component along $z$

$u_x$	velocity component fluctuation along $x$
$u_y$	velocity component fluctuation along $y$
$u_z$	velocity component fluctuation along $z$
$V_i$	vertical velocity component of camera $i$ , $i = \{1,2\}$
$W_s$	spanwise drift velocity
$\bar{x}$	vector position
$(x,y,z)$	Cartesian coordinates
$\alpha_1, \alpha_2$	camera position angles inside the $(x,z)$ plane
$\beta_1, \beta_2$	camera position angles inside the $(y,z)$ plane
$\Gamma_2$	vortex identification criterion
$\delta$	difference
$\varepsilon_i$	velocity accuracy for camera $i$ , $i = \{1,2\}$
$\varepsilon_{(x,y)}$	velocity error in the $(x,z)$ plane
$\varepsilon_{(x,z)}$	velocity error in the $(x,z)$ plane
$\varepsilon_{U,x}$	accuracy for the $x$ velocity component
$\varepsilon_{U,y}$	accuracy for the $y$ velocity component
$\varepsilon_{U,z}$	accuracy for the $z$ velocity component

## 1 Introduction

PIV is a measurement technique which is valuable for quantitative flow description (Adrian, 1991, Raffel et al., 1998). Thanks to the development of high-speed cameras and high repetition rate lasers, it is now possible to explore turbulent flows. Observation of laser plane (2D) with two cameras provides the field of three components of velocity (3C). Stereoscopic PIV algorithm implemented for this study is an optical flow using dynamical programming. It is an advanced PIV algorithm (Lecordier and Trinité, 2003) which has been evaluated and is particularly adapted for flows with large velocity gradients. The first aim of the study is to carry out 3C-2D PIV measurements on a cavity flow to test the PIV algorithm in a real wall-bounded flow configuration. The second objective is to get the flow structure within the cavity to get the averaged velocity with components of Reynolds tensor and better understand the spanwise development of instabilities.

Cavity flows are a wide class of wall-bounded flows dominated by recirculation vortices. It is possible to discriminate between lid-driven cavity flows (Migeon, 2000, Guermont et al., 2002, Migeon, 2002, Migeon et al., 2003), and shear-layer cavity flows (Fang et al., 1999, Lin and Rockwell, 2001, Forestier et al. 2003, Larchevêque et al., 2004, Kegerise et al., 2004, Haigermoser et al., 2009). Among these latter, it is worth distinguishing, after Charwar et al. (1961), between open cavities, where the shear-layer interacts with the downstream edge of the cavity, and closed cavities with flow reattachment on the cavity bottom. The boundary between these two classes is found for a cavity length to depth ratio varying from 8 (Sarohia, 1977) to 11 (Charwar et al. 1961). Hereafter, the configuration considered is a shear-layer open cavity flow. Most of the previous studies focused on the shear layer mode and the cavity resonance frequency (Knisely and Rockwell, 1982, Neary and Stephanoff, 1987, Chatellier et al. 2004). However, the shear layer instability is not the only instability observed in cavity flows. Direct numerical simulation (Brès 2007, Brès and Colonius, 2008) of compressible flows over open cavities shows a three-dimensional internal flow motion. This 3D flow motion was also observed on flow visualizations (Faure et al. 2007, Faure et al. 2009-a). The present measurements are conducted in order to provide quantitative experimental information on the velocity field inside the cavity and to catch the structure in a configuration where the centrifugal instability is developed.

After a description of the experimental set-up and apparatus, the PIV system calibration procedure is exposed, permitting the localization of the two cameras relatively with the laser plane. A comparison between 2C-2D PIV and 3C-2D PIV is given to validate the use of a

stereoscopic algorithm on this type of flow. Measurements in two orthogonal planes are explored to understand the global 3D flow dynamics. The main flow features and development of a Taylor-Görtler-like instability are also discussed.

## 2 Experimental set-up and apparatus

The airflow is generated by a centrifugal fan placed upstream of a settling chamber (Figure 1 a). The seeding particle injection is achieved at the fan inlet. An axial duct terminated with honeycomb and a contraction drives the flow towards the experimental facility, which consists of a test section containing a flat plate, beginning with an elliptical leading edge, in order to fix the boundary layer origin. The cavity span  $S = 300$  mm is constant because the cavity ends in this direction are the wind tunnel vertical walls (Figure 1 b). These ends will be referred to “cavity lateral sides” hereafter. The two cavity heights considered in this study are  $D = 25$  mm (providing a span ratio  $S/D = 12$ ) and  $D = 50$  mm ( $S/D = 6$ ). Lengths are changed between 25 mm and 75 mm. The cavity length  $L$  and depth  $D$  define aspect ratio  $L/D$ , cavity aspect ratios  $L/D = 1, 1.25$  and  $1.5$  are studied hereafter. The  $x$ -axis is the external flow direction, the  $y$ -axis is the cavity depth direction and the  $z$ -axis is the cavity span direction. The flow is considered for Reynolds numbers, based on external flow velocity  $U_e$  and cavity depth  $D$ , around 2300 to 3800. Hereafter, the expressions “upstream” and “downstream” will refer to the external velocity direction. The origin of the Cartesian coordinate system is placed at the upstream edge of the cavity at mid-span. PIV measurements are conducted with two pulsed YAG lasers emitting at 532 nm. The first laser, used for visualizing a  $(x,z)$  plane, is flashing 250 mJ per pulse during 8 ns, while the second one, used for visualizing a  $(x,y)$  plane, is flashing 30 mJ during 6 ns. Measurements are recorded simultaneously in the two orthogonal planes, but the present analysis focuses on the average and standard deviation of velocity fields. The frame recording system consists of 10-bit cameras with  $1032 \times 778$  pixels and a frequency of 20 Hz. The maximum angle of the field of view observed by the cameras is less than 13 deg, which leads to a maximum parallax aberration of 2.5% on the component orthogonal to the measurement plane. The  $(x,y)$  plane situated at  $z/S = 0.25$  is explored with one camera aligned with the cavity span axis, allowing a comparison with the 2C-2D PIV optical flow algorithm (Figure 2 a). The laser plane location is not chosen at the cavity midspan in order to avoid a symmetry plane. In that configuration, cameras are placed on Scheimpflug mounts, which allows an angle of 45 deg between them. A  $(x,z)$  plane situated at  $y/D = -0.3$  is also studied for a complete description of the three-dimensional flow motion (Figure 2 b). For that measurement, the angle between the two cameras is limited to 20 deg in order to perform a stereoscopic PIV measurement without Scheimpflug mounts. This is justified because a complete view of the cavity span requires a reduction of the angle between the two cameras. The final setting is the result of a compromise between the frame focusing, which decreases with the angle, and the accuracy of the velocity component orthogonal to the laser plane, which increases with the angle. This point will be discussed in part 5. As the largest velocity component is perpendicular to the  $(x,z)$  plane, the laser sheet thickness is enlarged to 2 mm to reduce the loss of particle image pairing between the two flashes.

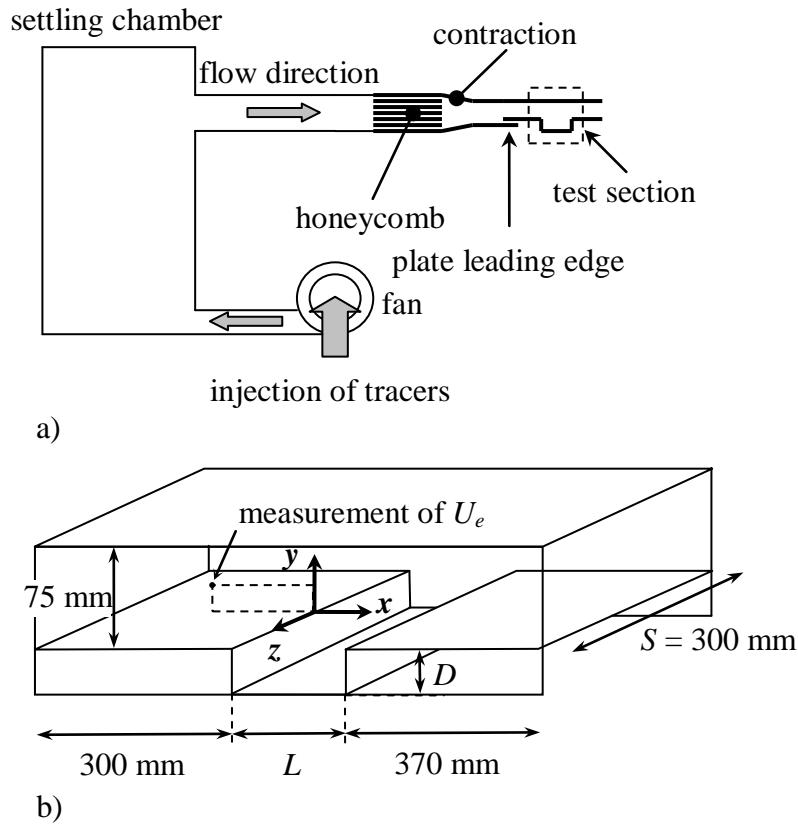


Figure 1: Experimental set-up: a) wind tunnel, b) test section dimensions and coordinates system.

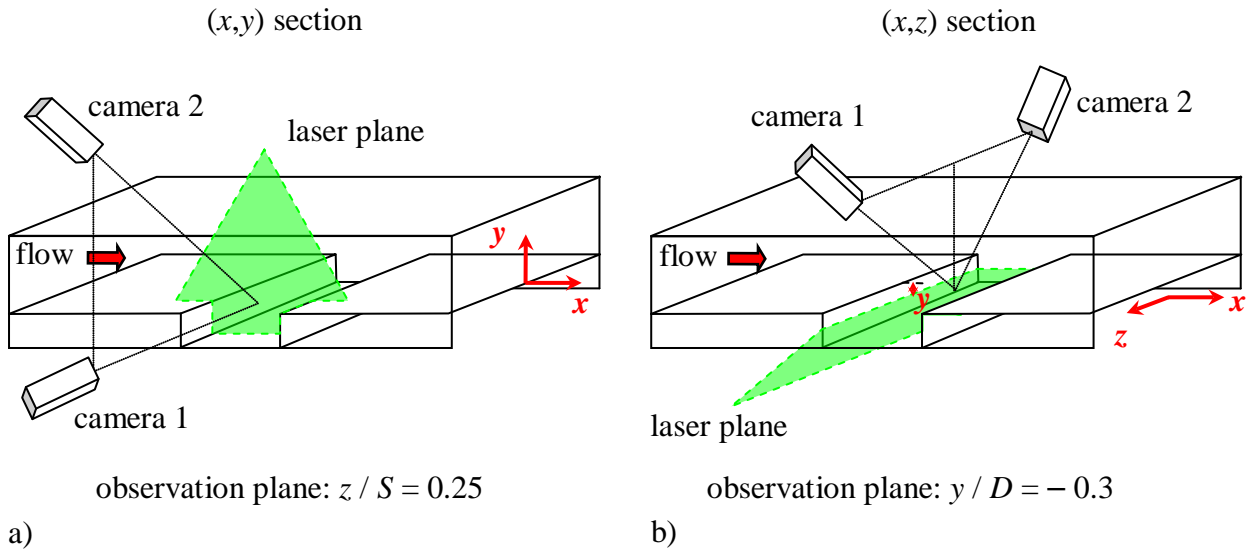


Figure 2: Stereoscopic system: a) measurements in a (x,y) section, b) measurements in a (x,z) section.

### 3 PIV algorithm

Optical flow is an alternative computation method to cross-correlation algorithms, for velocity field calculation, providing a dense velocity field from two consecutive frames (Corpetti et al., 2006). It is based on the assumption of brightness constancy of particle images between these two frames. Many methods have been proposed in the last two decades to estimate such an optical

flow, most of them based on the work of Horn and Schunck (1981). In the present work, computations of PIV frames are not based on Horn and Schunck (1981) but analyzed with an optical flow algorithm using orthogonal dynamic programming (Quénot et al., 1998). It has been successfully evaluated in the Second and Third International PIV Challenges (Stanislas et al., 2005, Stanislas et al., 2008) and exhibits very small bias and also has been identified as the most accurate in the boundary layer (Stanislas et al., 2005) and more broadly one of the best algorithm in strong gradient area. The optical flow used in this work is then particularly suitable for measurement inside a cavity flow mainly organized around strong gradient velocity features. This advanced PIV method is based on an iterative search of a global alignment of particle images, with regularity and continuity constraints (minimization of a Minkowski norm). The particle image displacement problem inside a plane is reduced to a one-dimension problem, considering the displacement in one direction within a given analysis strip. The two-dimensional solution is obtained by successive iterative resolution within smaller and smaller orthogonal strips. The main advantages of this iterative algorithm are:

- to be particularly stable, especially in noisy images processing with a low spatial definition, making available cheap cameras sets;
- to present an accuracy comparable to the best advanced algorithms based on cross-correlation using adaptive meshes;
- to be used for sequences of more than two frames in the case of regularly time sampled sequences (high speed PIV);
- to provides highly resolved displacement fields up to one vector per pixel keeping the computation time per vector reasonable;
- velocity field is by construction continuous and differentiable, which is particularly adapted for strong velocity gradient flows;
- it can be generalized to stereoscopic PIV to provide three velocity components, this version of the algorithm being the object of this study.

Its principal drawbacks are:

- large computation time without exceeding advanced algorithms using cross-correlation and frame deformation (Scarano, 2001);
- a sensitivity to local out of plane velocity component in the two-component version of the algorithm (Stanislas et al., 2005);
- adjustment of many parameters and their sensitivity to flow configuration.

The stereoscopic version of the PIV optical flow algorithm is implemented in this work. The optical flow resolution with the image analysis setting used is  $1 / 32^{\text{nd}}$  pixel. For the present case and actual magnification, that resolution corresponds, for measurements in a  $(x,y)$  plane, to a velocity accuracy of  $3 \cdot 10^{-3} \text{ m} \cdot \text{s}^{-1}$  and a relative accuracy  $\varepsilon_{(x,y)} = 0.32\%$ . For measurements in a  $(x,z)$  plane, that accuracy is  $2.2 \cdot 10^{-4} \text{ m} \cdot \text{s}^{-1}$  and a relative accuracy  $\varepsilon_{(x,z)} = 0.11\%$ . To improve the frame quality before PIV algorithm treatment, a filtering method was implemented in the course of this work. During the experiment setting, particular attention is devoted to laser light positioning and to the suppression of all the undesirable light reflections. However, some wall reflections remain in the recorded frames, and can alter the PIV processing (Figure 3 a). In order to get rid of these optical noise sources, it seems easy to subtract from a frame with flow, a frame recorded without flow, where only undesirable reflections are present, referred to as background frame (Figure 3 b). In addition, the recording frames include not only the cavity, but also some part of the external upper flow, and as a consequence the cavity walls are inside the viewed field. In order to suppress any light reflection which would affect the PIV algorithm, a mask is applied to the zone which is not the flow itself, where no image tracer should be found (Figure 3 c). The subtraction of a raw frame to the background frame and the mask provide a filtered frame (Figure 3 d). The energy distribution of the laser sheet generates a non-uniformity of illumination, and the tracers are not scattering the same amount of light. Then, a high-pass filter is finally applied on

PIV frames to equalize particles illumination in agreement with the assumption of the optical flow approach (Figure 3 e, Quénot et al, 1998). That filtering is performed before the velocity field calculation.

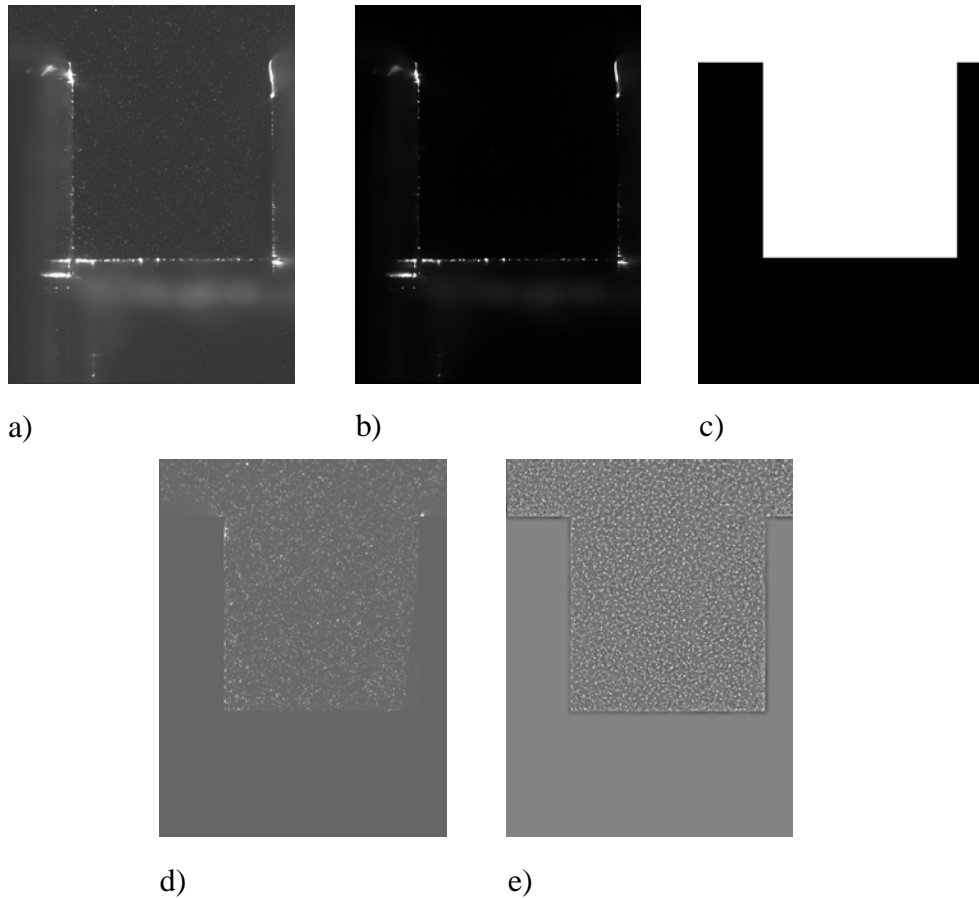


Figure 3: PIV frame filtering from camera 1 in the  $(x,y)$  setting: a) raw frame, b) background frame, c) masked zone, d) frame resulting of background frame and masked zone subtraction, e) high-pass filtering of the previous frame.

#### 4 Stereoscopic PIV calibration

The calibration of the two cameras is included in the procedure based on a pinhole model (Quénot et al., 2001). In order to accurately combine the 2C apparent velocity fields from the different viewpoints into a single 3C velocity field, an accurate camera model giving the correspondence between the actual target coordinate system and the camera sensor location is required from each viewpoint. This relationship is usually modeled by functions whose parameters are evaluated from the analysis of several images of the target, placed at different locations parallel to the laser sheet (Scarano et al., 2005). The main drawback of this method is the need to take several images while placing the target very accurately at the desired positions. Moreover, the result may be unstable relative to non parallel and not evenly spaced target locations. In the present procedure, each camera calibration is computed from a single view of a target placed in the laser plane and the camera focal length. In order to correct the possible deviation between the target and the lightening sheet, we perform an iterative search of the distance between the target optical center, and the actual position of the lightening plane.

#### 5 Velocity accuracy

Let's suppose that the exact position for each camera has been calculated from the previous calibration method. Then it is possible to consider the actual particle displacement inside the laser

sheet  $\delta x$ ,  $\delta y$ ,  $\delta z$  along the  $x$ ,  $y$ ,  $z$  axes. Each camera measures two velocity components inside a plane parallel to its sensor and obtained from the particle image displacement inside the laser sheet (Prasad, 2000, Westerweel et al 1996, Lawson and Wu, 1999, Callaud and David, 2004):

$$U_1 = \frac{\delta x + \delta z \tan \alpha_1}{\delta t} \quad V_1 = \frac{\delta y + \delta z \tan \beta_1}{\delta t}$$

$$U_2 = \frac{\delta x + \delta z \tan \alpha_2}{\delta t} \quad V_2 = \frac{\delta y + \delta z \tan \beta_2}{\delta t}$$

where  $\delta t$  is the time interval between two laser flashes and the angles  $\alpha_1$ ,  $\alpha_2$ ,  $\beta_1$ ,  $\beta_2$  the position angles of the two cameras in the  $(x,y,z)$  coordinate system (Figure 4). The expression for velocity components are provided by (Raffel *et al.*, 1998) and rewritten for the present configuration (Faure *et al.*, 2010):

$$U_x = \frac{U_1 \tan \alpha_2 - U_2 \tan \alpha_1}{\tan \alpha_2 - \tan \alpha_1}$$

$$U_y = \frac{V_1 \tan \beta_2 - V_2 \tan \beta_1}{\tan \beta_2 - \tan \beta_1}$$

$$U_z = \frac{U_1 - U_2}{\tan \alpha_1 - \tan \alpha_2} = \frac{V_1 - V_2}{\tan \beta_1 - \tan \beta_2}$$

If the cameras are positioned alongside  $y$ -axis, then angles  $\alpha_1$  and  $\alpha_2$  are small and a better estimate of the velocity components is given by (Figure 4):

$$U_x = \frac{U_1 + U_2}{2} - \frac{V_1 - V_2}{2} \frac{\tan \alpha_1 + \tan \alpha_2}{\tan \beta_1 - \tan \beta_2}$$

$$U_y = \frac{V_1 \tan \beta_2 - V_2 \tan \beta_1}{\tan \beta_2 - \tan \beta_1}$$

$$U_z = \frac{V_1 - V_2}{\tan \beta_1 - \tan \beta_2}$$

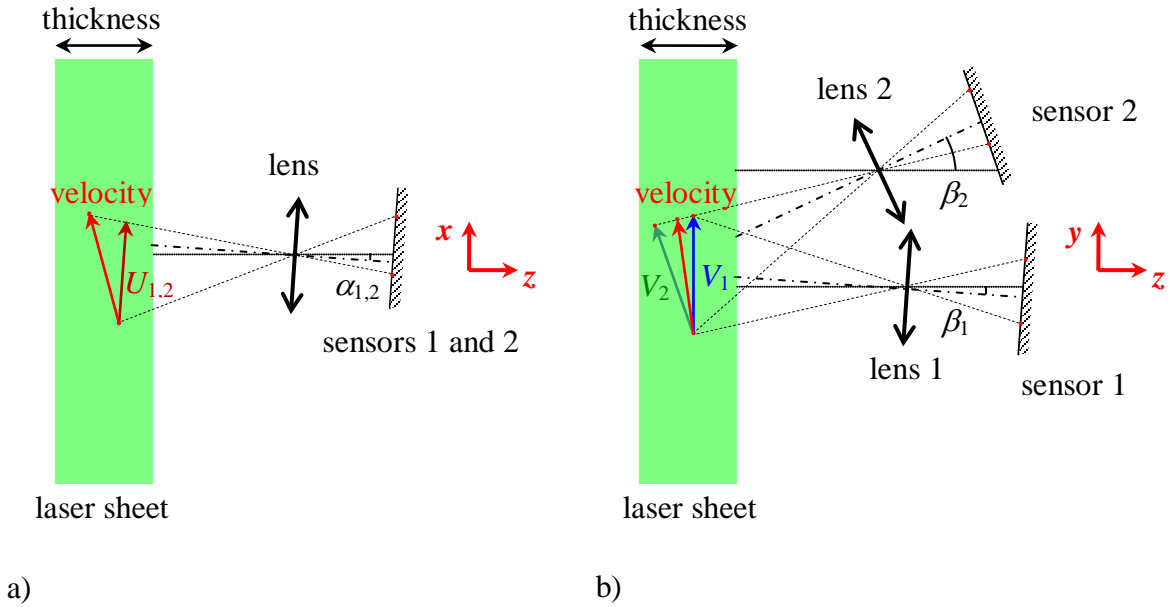


Figure 4: Stereoscopic PIV projection principle: a) viewed from the  $z$  direction, b) observed from the  $x$  direction.

Then, for measurements inside the  $(x,y)$  plane, if the measurement error is  $\varepsilon_1$  for the first camera and  $\varepsilon_2$  for the second camera and with angles  $\alpha_1 \sim \alpha_2 \sim \beta_1 \approx 0$  deg and  $\beta_2 \approx 45$  deg:

$$\varepsilon_{U,x} \approx \frac{\varepsilon_1 + \varepsilon_2}{2}$$

$$\begin{aligned}\varepsilon_{U,y} &\approx \varepsilon_1 \\ \varepsilon_{U,z} &\approx \frac{\varepsilon_1 + \varepsilon_2}{\tan \beta_2}\end{aligned}$$

Assuming  $\varepsilon_1 = \varepsilon_2 = \varepsilon$  yields to:

$$\varepsilon_{U,x} \approx \varepsilon_{(x,y)} = 0.32\% ; \varepsilon_{U,y} \approx \varepsilon_{(x,y)} = 0.32\% ; \varepsilon_{U,z} \approx 2\varepsilon_{(x,y)} = 0.64\%$$

With that setting, the relative accuracy on the velocity component orthogonal to the measurement plane is twice the accuracy of the other two components.

For measurements inside the  $(x,z)$  plane, with angles  $\alpha_1 \sim \alpha_2 \approx 0$  deg,  $\beta_1 \approx -10$  deg and  $\beta_2 \approx 10$  deg:

$$\begin{aligned}\varepsilon_{U,x} &\approx \frac{\varepsilon_1 + \varepsilon_2}{2} \\ \varepsilon_{U,y} &= \frac{\varepsilon_1 \tan \beta_2 + \varepsilon_2 \tan \beta_1}{\tan \beta_2 - \tan \beta_1} \\ \varepsilon_{U,z} &\approx \frac{\varepsilon_1 + \varepsilon_2}{\tan \beta_2 - \tan \beta_1}\end{aligned}$$

Assuming again  $\varepsilon_1 = \varepsilon_2 = \varepsilon$  we get:

$$\varepsilon_{U,x} \approx \varepsilon_{(x,z)} = 0.11\% ; \varepsilon_{U,y} \approx \varepsilon_{(x,z)} = 0.11\% ; \varepsilon_{U,z} \approx 6\varepsilon_{(x,z)} = 0.66\%$$

For present measurements in the  $(x,z)$  plane, the frame sharpness criterion is not strictly checked because we do not use Scheimpflug mounts between each camera sensor and lens. However, sharp enough frame recording is possible because of the choice of a small angle between the two cameras (20 deg). This limited angle is of course altering the resolution on the velocity component orthogonal to the  $(x,z)$  measurement plane.

## 6 Results

Comparison between standard 2C-2D PIV and stereoscopic 3C-2D PIV optical flow algorithms are given for measurements in the  $(x,y)$  plane and for configuration  $Re = 3750$ ,  $S/D = 12$  and  $L/D = 1$ . The first camera is set perpendicularly to the laser plane in order to calculate 2C-2D PIV fields and the second camera used for stereoscopic measurements forms an angle  $\theta \approx 45$  deg with the first camera axis (Figure 2 a). Both of them are placed on Scheimpflug mounts. The flow streamlines clearly identifies the vortex of spanwise axis inscribed inside the cavity (Figure 5 a-b). The instantaneous velocity profiles along the  $y$ -direction are given for three positions inside the cavity, respectively  $x/L = 0.25$ ,  $x/L = 0.54$  (line passing by the center of the recirculation vortex) and  $x/L = 0.84$  (Figure 5 c, d, e). For each profile, the axial velocity  $U_x$  shows the large gradient between the external flow and the cavity around  $y = 0$  mm and the negative velocity in the cavity bottom, corresponding to the clockwise flow rotation of the recirculation vortex. Note that the axial velocity presents larger negative values near the cavity bottom, for  $x/L = 0.54$  which correspond to vertical line passing by the vortex center, where the velocity is purely axial. Similar comments are valid for the vertical velocity  $U_y$ , which is positive inside the cavity for  $x/L = 0.25$  (rise of the cavity flow), zero for  $x/L = 0.54$  along the vertical line passing by the vortex center, and negative for  $x/L = 0.84$  (dive inside the cavity). This velocity component is close to zero at the cavity top and bottom where the flow direction is the  $x$ -axis. There is a good agreement between the two algorithms with a little stronger noise on 3C-2D PIV due to the geometrical projection on velocity estimates resulting from two observation directions. A statistical convergence with an error lower than 1% has been found from the average of 200 PIV fields, but the results given below are obtained by averaging at least 500 instantaneous fields. The averaged velocity is given in Figure 6 for the same configuration. The axial and vertical velocities are matching very well between the two algorithms. The global trends observed in instantaneous field are also present in the averaged velocity field. The profiles obtained from averaged velocity fields

do not show effects of perspective error. Note that the flow structure is completely different from Özsoy et al (2005) where the cavity aspect ratio is  $L/D = 4$ .

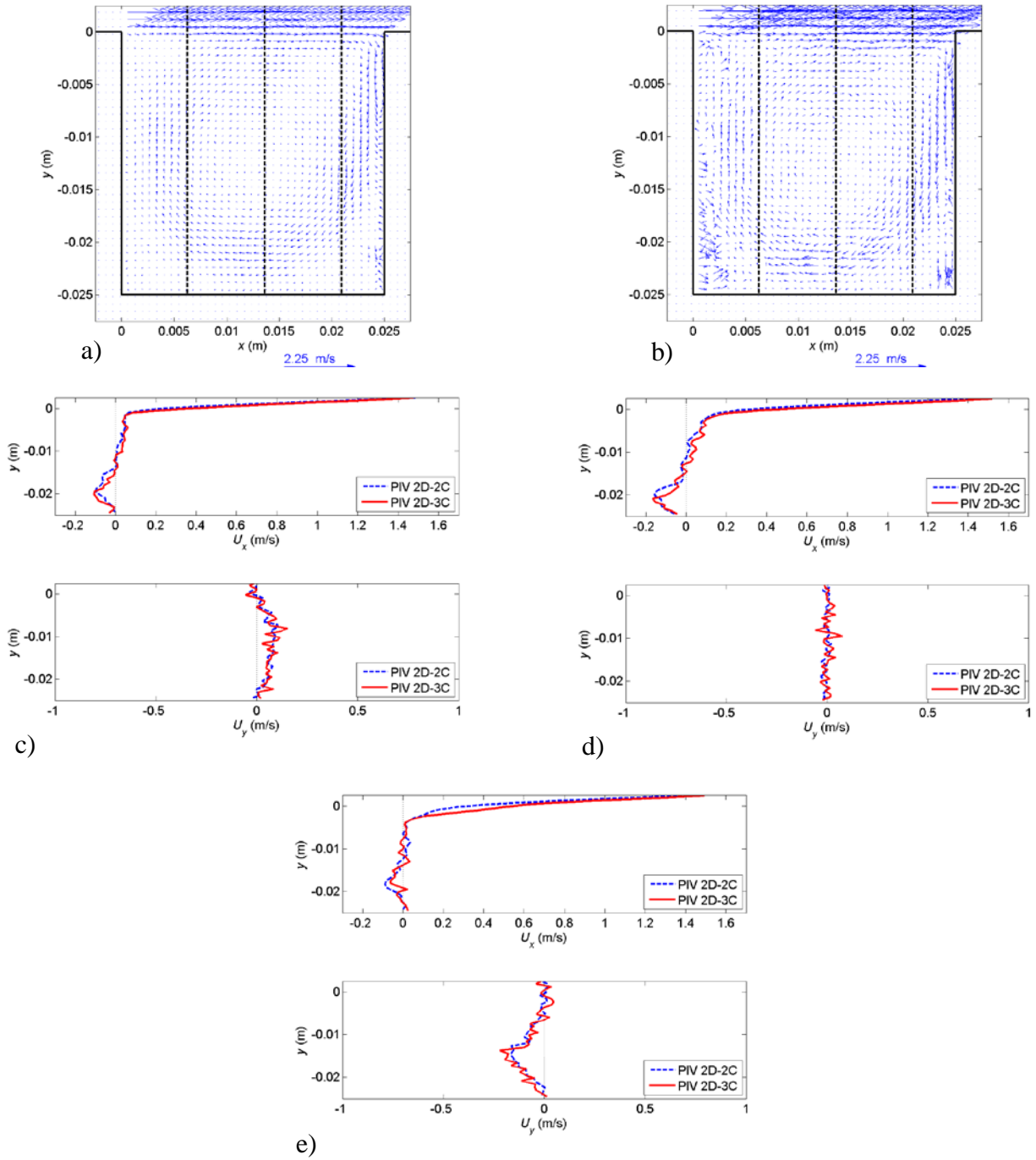


Figure 5: Comparison of instantaneous velocity fields obtained with 2C-2D PIV and 3C-2D PIV for  $Re = 3750$  ( $U_e = 2.25 \text{ m}\cdot\text{s}^{-1}$ ),  $S/D = 12$ ,  $L/D = 1$ ,  $y/D = -0.3$ : a) streamlines 2C-2D PIV, b) streamlines 3C-2D PIV; and velocity profiles for three positions inside the cavity: c)  $x/L = 0.25$ , d)  $x/L = 0.54$  (center of the recirculation vortex) and e)  $x/L = 0.84$ .

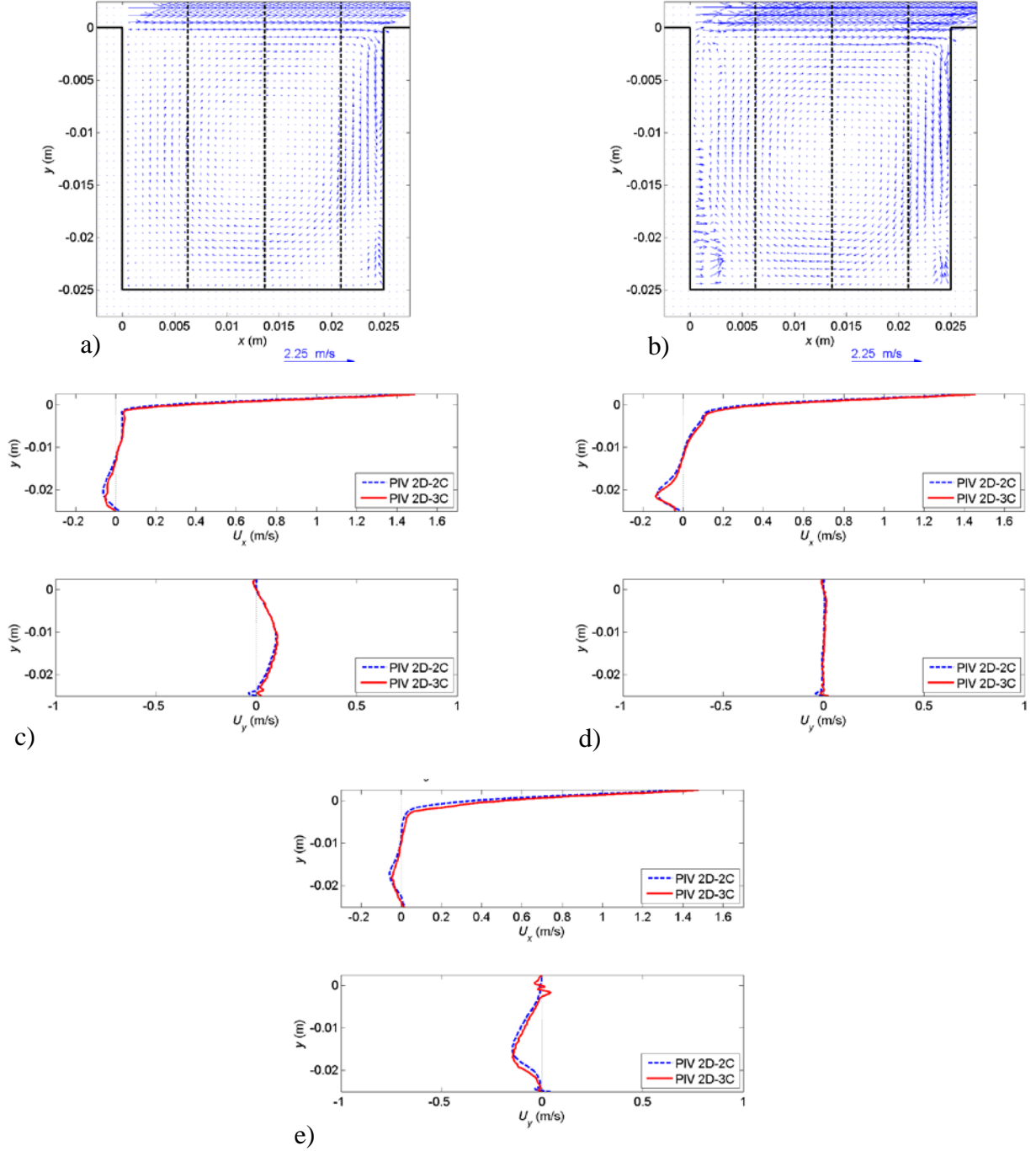


Figure 6: Comparison of the average of 500 velocity fields obtained with 2C-2D PIV and 3C-2D PIV for  $Re = 3750$  ( $U_e = 2.25 \text{ m}\cdot\text{s}^{-1}$ ),  $S/D = 12$ ,  $L/D = 1$ ,  $y/D = -0.3$ : a) streamlines 2C-2D PIV, b) streamlines 3C-2D PIV; and mean velocity profiles for three positions inside the cavity: c)  $x/L = 0.25$ , d)  $x/L = 0.54$  (center of the recirculation vortex) and e)  $x/L = 0.84$ .

The discussion of the flow morphology in two different orthogonal planes inside the cavity is present hereafter for  $Re = 2967$ ,  $S/D=6$  and  $L/D=1.25$ . Results for  $z/S = 0.25$  are given in Figure 7. A laser reflection on one of the camera leads to spurious velocities around  $(x = 0.01 \text{ m}, y = -0.015 \text{ m})$ , which are not presented in the figure. The evidence of the recirculation motion inside the cavity is shown with positive  $U_x$  above the cavity (the axial velocity saturates the color map in the external flow), and negative  $U_x$  at the cavity bottom (Figure 7 a). Similarly, negative  $U_y$  are found near the downstream cavity edge and positive  $U_y$  near the upstream cavity edge (Figure 7 b). Despite the frame filtering procedure, measurements are affected by remaining reflections in

the wall vicinity. Light reflections are also observed in the downstream wall which affects particularly the transverse velocity. This  $U_z$  component exhibits positive levels near the upstream cavity edge while negative levels are found near the downstream edge (Figure 7 c). That negative  $U_z$  region is associated with the flow motion towards the opposite lateral cavity side. The noise observed in the  $U_z$  component results in the larger measurement error caused by the projection setting.

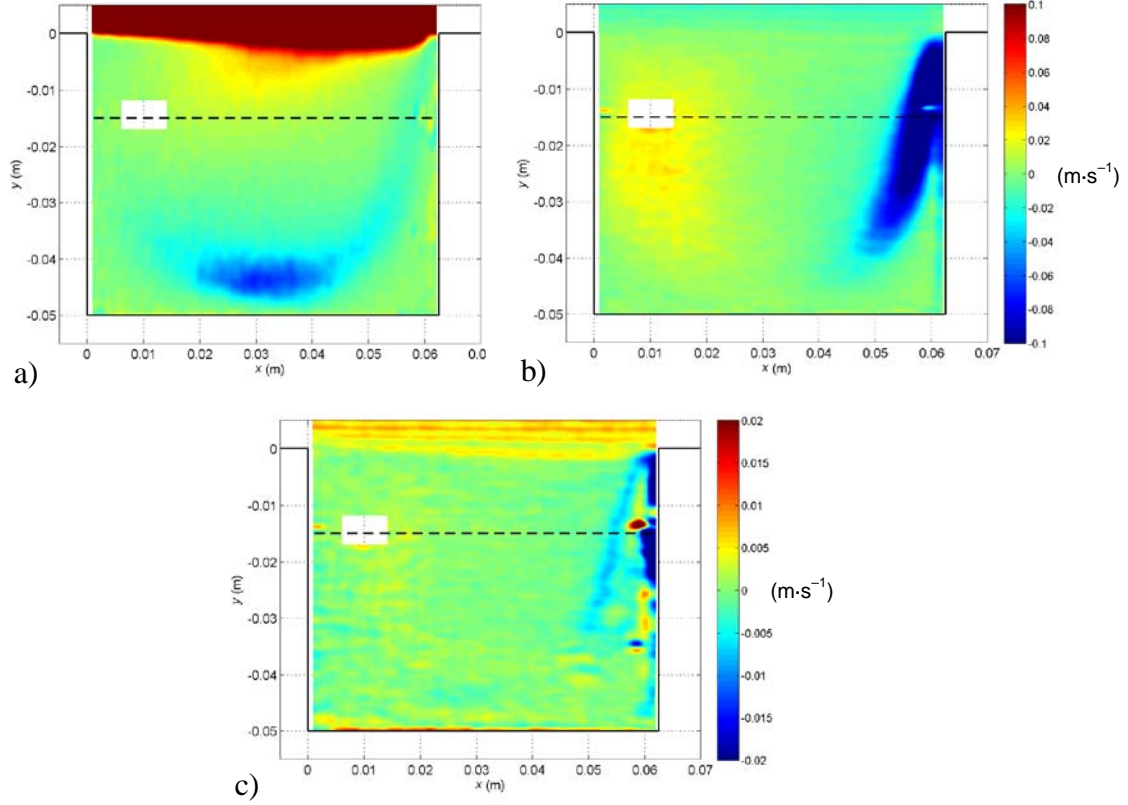


Figure 7: Averaged velocity components obtained with 500 PIV fields inside a  $(x,y)$  plane for  $Re = 2967$  ( $U_e = 0.89 \text{ m}\cdot\text{s}^{-1}$ ),  $S/D=6$ ,  $L/D=1.25$ : a)  $U_x$ , b)  $U_y$ , c)  $U_z$ , the dashed line corresponds to the  $(x,z)$  plane of measurements.

Measurements are also made inside a  $(x,z)$  plane situated at  $y/D = -0.3$  (Figure 2 b) to understand the global 3D flow features and the development of a row of Taylor-Görtler-like counter-rotating vortices. As the cavity flow is three-dimensional, and dominated by the primary vortex motion, the PIV fields inside the  $(x,z)$  plane are carried out with a large velocity component perpendicular to the measurement plane, whose velocity is 5 times larger than the velocity of Taylor-Görtler-like centrifugal vortices. Then, a two-component measurement is subject to projection effect away from the optical axis, which justifies the use of stereoscopic PIV. The instantaneous field of the  $U_x$  component shows maximum values in the central part of the cavity with span modulations correlated with the position of the quasi-annular Taylor-Görtler-like centrifugal vortices (Figure 8 a). The flow near the upstream edge of the cavity rather shows positive values of  $U_y$  while the downstream edge of the cavity rather shows negative values of  $U_y$ , both corresponding to the recirculation motion of the vortex of spanwise axis (Figure 8 b). Note that  $U_y$  is represented with a different color scale because its maximum values are larger than the other two components. Furthermore, this component is orthogonal to the laser plane and its estimate is six times larger than the error on  $U_x$  and  $U_z$ . The  $U_z$  component presents larger positive levels in the left part of the cavity, and larger negative levels in the right (Figure 8-c). The velocity scattering in instantaneous velocity fields is smoothed by time-averaging on 1000 fields (Figure 9). The

averaged  $U_x$  component shows maximum values in the central part of the cavity without span modulations previously observed, evidence of a time migration of Taylor-Görtler-like centrifugal vortices (Figure 9 a). However, the right part of the cavity measurement plane shows larger values than the left part, suggesting a flow dissymmetry. The averaged field of  $U_y$  (Figure 9 b) presents positive values near the upstream edge of the cavity and negative values near the downstream edge, but the large variations along the  $z$  axis observed on the instantaneous field are smoothed. This is confirming the primary vortex motion developing inside the cavity where the flow rises near the upstream cavity edge and dives near the downstream cavity edge. The averaged  $U_z$  component (Figure 9 c) is positive on the left and negative on the right, with maximum levels near the lateral cavity wall, suggesting a flow motion from these walls towards the cavity centerline ( $z = 0$ ). This is the confirmation of a Bödewadt pumping (Bödewadt, 1940), previously observed on flow visualizations (Faure et al., 2009-a). This Bödewadt pumping is the result of two spiral vortices, located near the lateral sides of the cavity ( $z = \pm 0.15$  m), which create a flow along the recirculation vortex axis, towards the cavity centerline ( $z = 0$  m). The present work is the evidence, on velocity fields obtained with PIV, of the transverse flow motion, organized in the  $(x,z)$  plane in four recirculation cells.

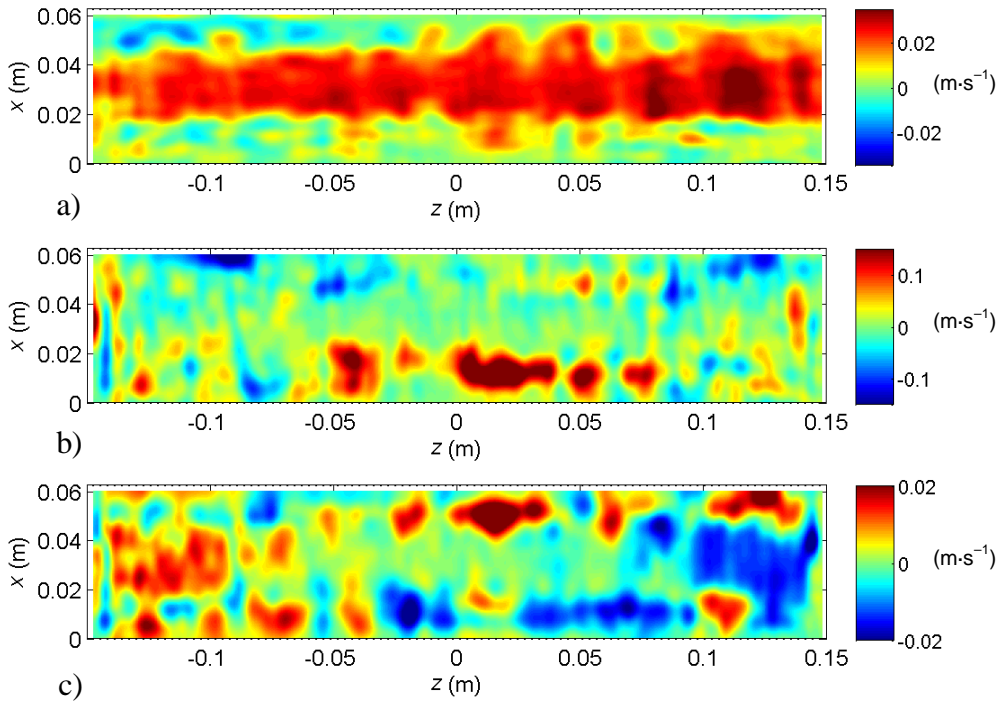


Figure 8: Instantaneous velocity components inside a  $(x,z)$  plane for  $Re = 2967$  ( $U_e = 0.89 \text{ m}\cdot\text{s}^{-1}$ ),  $S/D=6$ ,  $L/D=1.25$ : a)  $U_x$ , b)  $U_y$ , c)  $U_z$ .

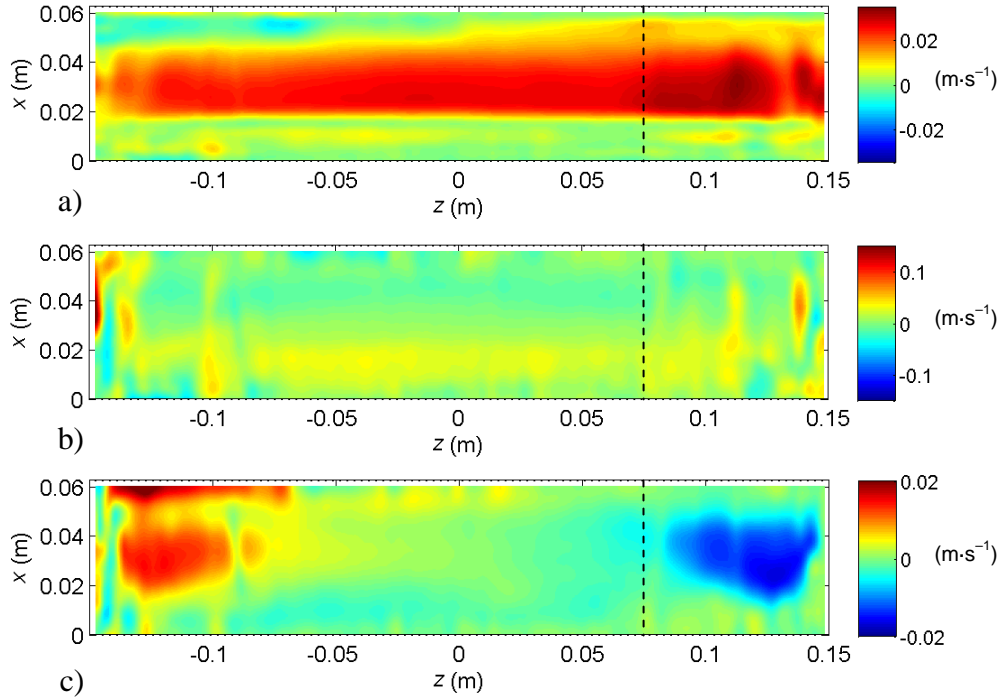


Figure 9: Averaged velocity components obtained with 1000 PIV fields inside a  $(x, z)$  plane for  $Re = 2967$  ( $U_e = 0.89 \text{ m}\cdot\text{s}^{-1}$ ),  $S/D=6$ ,  $L/D=1.25$ : a)  $U_x$ , b)  $U_y$ , c)  $U_z$ , the dashed line corresponds to the  $(x, y)$  plane of measurements.

The standard deviation and covariance of velocity fluctuations inside a  $(x, z)$  plane situated at  $y/D = -0.3$  are presented in Figure 10. The maxima are observed near the upstream and downstream cavity edges, while the value is close to zero in the central part of the cavity, observed inside the measurement plane. We can deduce that the zones of maximum energy are associated with the strong velocity gradient created by the mean flow interacting with upstream and downstream cavity walls. Higher levels of standard deviations are found near the downstream cavity edge, where the shear-layer injects momentum and interacts with the downstream cavity wall. Note that the covariance of velocity fluctuations along  $y, z$  and  $x, z$  is positive on the left and negative on the right, representing the shear flow along the  $z$  axis and the flow dissymmetry resulting of different flow establishment conditions. Nevertheless, as one could expect, the change of sign of these two quantities does not occur for the cavity centerline ( $z = 0$  m) but is shifted on the right (around  $z = 0.08$  m). This observation is confirming the flow dissymmetry observed on the averaged axial velocity, and is discussed below in relation with the Taylor-Görtler vortices spanwise drift.

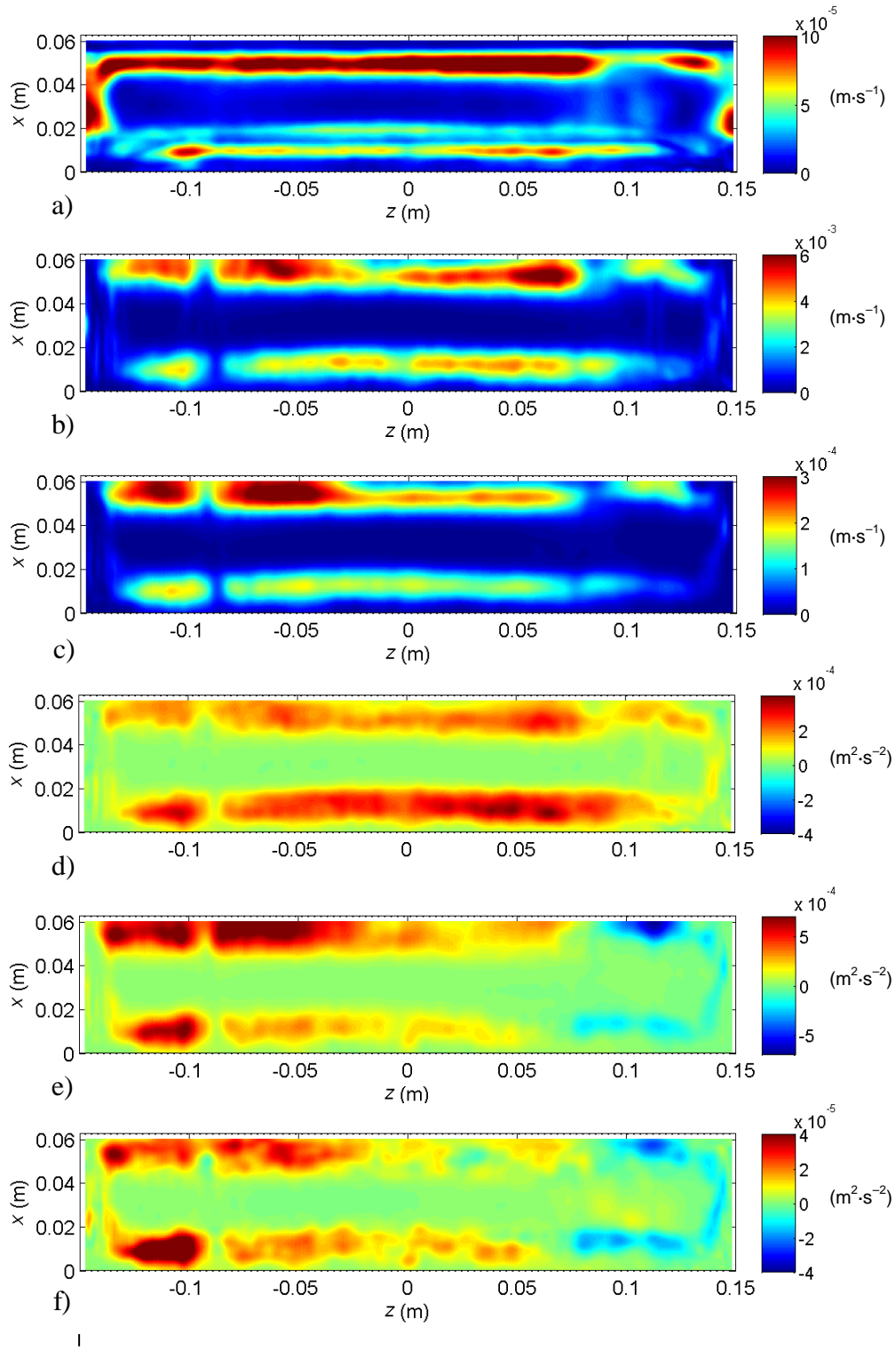


Figure 10: Standard deviations and covariances of the velocity fluctuations obtained with 1000 PIV fields inside a  $(x,z)$  plane for  $Re = 2967$  ( $U_e = 0.89 \text{ m}\cdot\text{s}^{-1}$ ),  $S/D=6$ ,  $L/D=1.25$ : a)  $\sqrt{u_x^2}$ , b)

$$\sqrt{u_y^2}, \text{ c) } \sqrt{u_z^2}, \text{ d) } \overline{u_x u_y}, \text{ e) } \overline{u_y u_z}, \text{ f) } \overline{u_x u_z}.$$

## 7 Vortex identification

These stereoscopic measurements also validate previous analyses conducted with two-component PIV, about the size and wavelength of centrifugal vortices identified for some parameters (Faure et al., 2008). Above a threshold, a row of pairs of counter-rotating vortices appears inside the cavity. In order to locate the vortices, the  $\Gamma_2$  criterion is applied (Graftieaux et al., 2001, Michard & Favelier, 2004). It is an Eulerian criterion which is a normalized kinetic moment, considering the relative motion around a given position, defined as:

$$\Gamma_2(\bar{x}) = \frac{1}{A} \int_{\bar{x}' \in A} \frac{(\bar{x}' - \bar{x}) \wedge [\vec{U}(\bar{x}') - \vec{U}(\bar{x})]}{\|\bar{x}' - \bar{x}\| \|\vec{U}(\bar{x}') - \vec{U}(\bar{x})\|} d\bar{x}'$$

In this equation,  $A$  is a domain containing the position  $\bar{x}$ . The main advantage of this criterion over other identification tools is that it is Galilean invariant, thus it is able to track a moving vortex and it is particularly adapted to point out vortices from experimental data with measurement noise in comparison with vorticity. It is applied on instantaneous fields and underlines the location of the pairs of counter-rotating vortices associated with zones where it is close to  $-1$  or  $1$  according to the clockwise or anticlockwise rotation direction (Figure 11). The Taylor-Görtler row observed in flow visualizations (Figure 12) near the upstream and downstream cavity edge (Faure et al., 2009-a) and 2D-2C PIV measurements (Faure et al., 2009-b) are also observed in the central part of the cavity as blue spots alternately with red spots of  $\Gamma_2$ . Note that streak lines observed in flow visualizations are different from the streamlines of the velocity field and the  $\Gamma_2$  criterion, but both of these fields clearly identify the row of Taylor-Görtler-like vortices. In addition, in flow visualization, no pattern associated with Taylor-Görtler vortices is identified in the central part of the cavity. The same behavior is observed for the considered configuration,  $Re = 2967$ ,  $S/D=6$ ,  $L/D=1.5$ . The instantaneous field of velocity fluctuations, obtained with mean velocity field subtracted, shows larger vectors near the cavity upstream and downstream edges, where vortices are observed (Figure 13). The field of  $\Gamma_2$  presents red and blue patterns associated with clockwise and anticlockwise vortices, with vortices getting tangled up in the left part of the cavity (Figure 14).

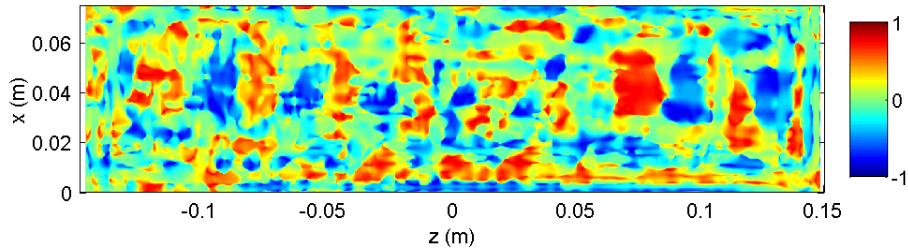


Figure 11: Instantaneous field of the  $\Gamma_2$  criterion inside a  $(x,z)$  plane for  $Re = 2967$  ( $U_e = 0.89$   $\text{m}\cdot\text{s}^{-1}$ ),  $S/D=6$ ,  $L/D=1.5$ .

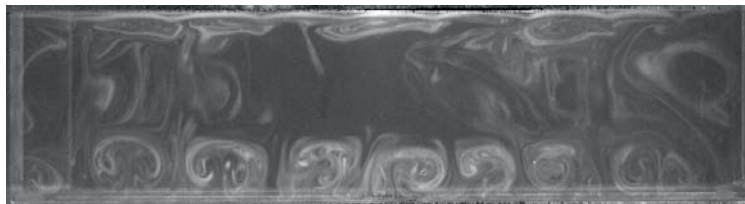


Figure 12: Flow visualization inside a  $(x,z)$  plane for  $Re = 2967$  ( $U_e = 0.89$   $\text{m}\cdot\text{s}^{-1}$ ),  $S/D=6$ ,  $L/D=1.5$ .

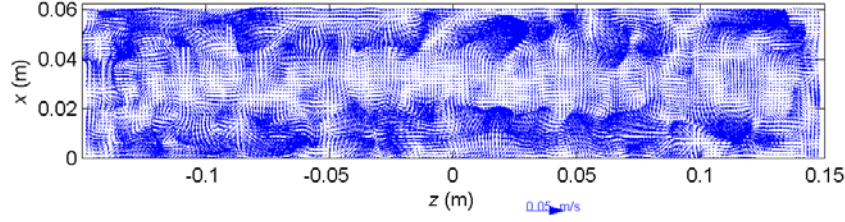


Figure 13: Instantaneous field of the velocity fluctuations inside a  $(x,z)$  plane for  $Re = 2967$  ( $U_e = 0.89 \text{ m}\cdot\text{s}^{-1}$ ),  $S/D=6$ ,  $L/D=1.25$ .

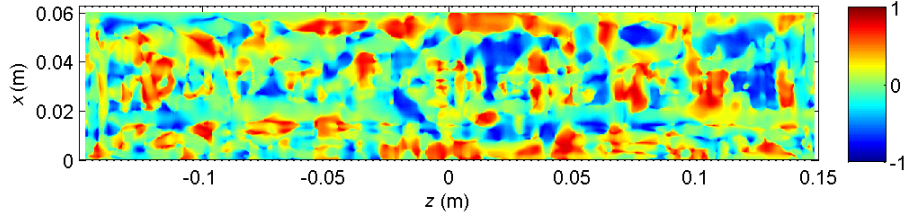


Figure 14: Instantaneous field of the  $I_2$  criterion, for the very same time as Figure 13, inside a  $(x,z)$  plane for  $Re = 2967$  ( $U_e = 0.89 \text{ m}\cdot\text{s}^{-1}$ ),  $S/D=6$ ,  $L/D=1.25$ .

We have seen in Figure 9 that recirculation cells observed in the  $(x,z)$  plane allow Taylor-Görtler-like vortices to drift towards the cavity sides. Note that the spanwise drift velocity  $W_s$  can be considered as a phase velocity of the Taylor-Görtler-like vortices which is different from  $U_z$  which is the flow velocity (Figure 9 c). That spanwise drift velocity is measured considering a quantity representing the vortices from space-time diagrams. They are built stacking over each other a horizontal line of the  $I_2$  field chosen in a region where a row of vortices is present, at different successive times. On such diagrams, vertical lines are associated to stationary events, while oblique lines are associated to traveling patterns (Figure 15). Thus, the time development of  $I_2$  allows tracking the motion of these vortices. If oblique stripes are moreover straight lines, it means that the pattern is traveling at a constant velocity. This is the case in the left part of the cavity, while some pairs of vortical structures are developing in the right towards the cavity side. As the  $I_2$  diagram oblique lines are associated with vortices migrating with a constant velocity, they can be characterized, for each geometrical and flow configuration, with their higher slope corresponding to a spanwise drifting velocity  $W_s$ . The measurement of  $W_s/U_e$  brings to  $0.0092 \pm 0.002$  for  $Re = 2967$ ,  $S/D=6$  and  $L/D=1.25$ . The vertical stripes identified near  $z = \pm 0.15$  are associated with the corner spiral vortices which are the consequence of a fluid transport from the sides into the primary vortex core, due to the Bödewadt pumping and previously observed in lid-driven or open cavity flows (Chiang et al. 1997, Migeon et al. 2003, Faure et al. 2009). These corner spiral vortices were not observed for  $S/D=6$  in the latter reference initiating flow visualizations on the very same experimental setting, because the seeding of lateral cavity sides was difficult. The strong flow dissymmetry observed inside the cavity present a flow symmetry axis located at  $z = 0.08 \text{ m}$ , which corresponds to the symmetry line of the covariance of velocity fluctuations along  $y, z$  and along  $x, z$ . Pairs of counter-rotating vortices of stronger intensity seems to force the symmetry axis around  $z = 0.08 \text{ m}$ . A similar space-time diagram of  $I_2$  development inside the cavity is presented in Figure 16 for close parameters ( $Re = 2300$ ,  $S/D=6$ ,  $L/D=1.5$ ). The spanwise drift velocity is  $W_s/U_e = 0.013 \pm 0.002$  which is the same order in magnitude of the velocity previously obtained from flow visualizations, respectively  $W_s/U_e = 0.010 \pm 0.002$  (Faure et al., 2009-a). Note in that figure the shift in the symmetry axis of migration of vortices on the right or left, situated near  $z = -0.02 \text{ m}$ . However, the previously observed pairs of vortices of stronger intensity located near  $z = 0.08 \text{ m}$  are still present, but they are not ordering the whole

spanwise drift motion anymore. Thus the cavity flow symmetry axis is very sensitive of geometry and flow parameters.

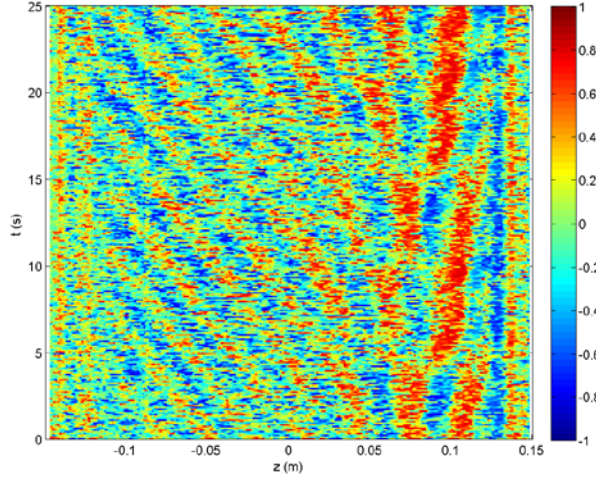


Figure 15: Space-time diagram for  $Re = 2967$  ( $U_e = 0.89 \text{ m}\cdot\text{s}^{-1}$ ),  $S/D=6$ ,  $L/D=1.25$  from a line extracted at  $x/L = 0.4$  inside the  $F_2$  field.

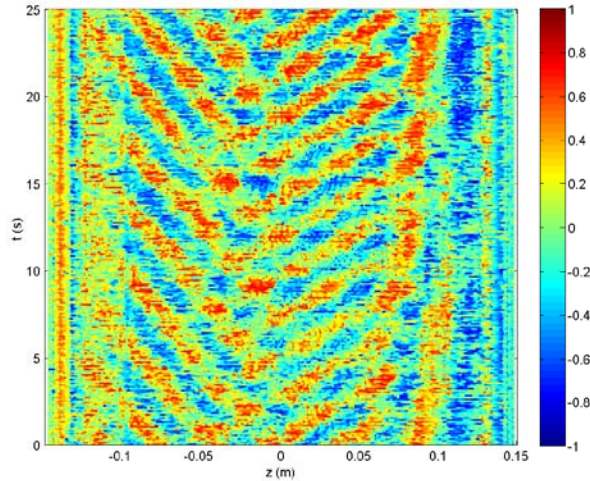


Figure 16: Space-time diagram for  $Re = 2300$  ( $U_e = 0.69 \text{ m}\cdot\text{s}^{-1}$ ),  $S/D=6$ ,  $L/D=1.5$  from a line extracted at  $x/L = 0.066$  inside the  $F_2$  field.

## 8 Conclusion

The three components of velocity have been investigated with a stereoscopic PIV optical flow technique in a wall-bounded cavity recirculation flow, for a configuration showing development of a Taylor-Görtler-like instability. The calibration of the two cameras is obtained using a single view of a plane target as well as the camera focal length and the sensor horizontal and vertical pixel sizes. The advantage of the method is that it is not necessary to take several views while placing the target very accurately at the desired positions and the result is not sensitive to non parallel and not evenly spaced target locations. Its main limitation is that it is based on a pinhole camera model which is not appropriate if the camera has significant non linear optical distortions and if there are changes of refraction index along the optical axis between the sensor plane and the target plane. Stereoscopic measurements provide three components of velocity field with an estimated error, for the  $(x,z)$  plane, six times greater for the component perpendicular to the plane,

and for the  $(x,y)$  plane, twice for the component perpendicular to the plane. For the first time, the spanwise drift of the Taylor-Görtler-like vortices has been observed experimentally from the velocity field and by the use of a vortex identification criterion, allowing forthcoming characterizations of the topology with cavity geometry and Reynolds number. The use of stereoscopic PIV has brought valuable information on the velocity component orthogonal to the measurement plane and the recirculation vortex dynamics. In addition, the flow symmetry sensitivity to geometry and Reynolds number has been demonstrated. The perspective of this work is a stability analysis of the recirculation centrifugal effects. The simultaneous stereoscopic PIV measurements in two orthogonal planes, in order to understand the coupling between the recirculating flow in the  $(x,y)$  plane, and the development of the Taylor-Görtler-like instability in the  $(x,z)$  plane would be also considered.

### Acknowledgement

The authors are indebted to the Direction Générale de l'Armement (DGA) for financial support of the work of Christelle Douay. They gratefully acknowledge Vincent Bourdin, Vincent Gautier and Yves Maire for their technical assistance on the experimental facility.

### References

- Adrian R (1991) Particle imaging techniques for experimental fluid mechanics. *Annual Rev Fluid Mech* 23:261–304
- Bödewadt U.T. (1940) Die Drehströmung über festem Grunde, *Z Angew Math Mech* 20 (5):241–253
- Brès GA (2007) Numerical simulation of three-dimensional instabilities in cavity flows, Ph.D. Thesis, California Institute of Technology, Pasadena, 149 p
- Brès GA, Colonius T (2008) Three-dimensional instabilities in compressible flow over open cavities, *J Fluid Mech* 599:309–339
- Callaud D, David L (2004) Stereoscopic particle image velocimetry measurements of the flow around a surface-mounted block, *Exp Fluids* 36:53–61
- Charwat AF, Roos JN, Dewey, FC, Hitz JA (1961) An investigation of separated flows. Part 1: the pressure field, *J Aero Sci* 28:457-470
- Chatellier L, Laumonier J, Gervais Y (2004) Theoretical and experimental investigations of low Mach number turbulent cavity flows, *Exp Fluids* 36:728–740
- Chiang TP, Hwang RR, Sheu WH (1997) On end-wall corner vortices in a lid-driven cavity. *J Fluids Eng* 119:201–204
- Corpetti T, Heitz D, Arroyo G, Mémin E, Santa-Cruz A (2006) Fluid experimental flow estimation based on an optical-flow scheme, *Exp Fluids* 40:80–97
- Fang LC, Nicolaou D, Cleaver JW (1999) Transient removal of a contaminated fluid from a cavity. *Intl J Heat Fluid Flow* 20:605–613
- Faure TM, Adrianos P, Lusseyran F, Pastur LR (2007) Visualizations of the flow inside an open cavity at medium range Reynolds numbers, *Exp Fluids* 42:169–184
- Faure TM, Defrasne A, Lusseyran F, Pastur LR (2008) Flow instabilities development inside an open cavity, 13<sup>th</sup> International Symposium on Flow Visualization, Nice (France), July 1-4 2008, Paper ID 81
- Faure TM, Pastur LR, Lusseyran F, Fraigneau Y, Bisch D (2009-a) Three-dimensional centrifugal instabilities development inside a parallelepipedic open cavity of various shape, *Exp Fluids* 47:395–410
- Faure TM, Lefèvre G., Pastur LR, Lusseyran F (2009-b) Critères d'apparition d'instabilités centrifuges dans une cavité ouverte, 19<sup>ème</sup> Congrès Français de Mécanique, Marseille (France), 24-28 août 2009

- Faure TM, Douay CL, Mochki S, Lusseyran F, Quénot G (2010) Stereoscopic PIV using optical flow: investigation of a recirculating cavity flow, 8<sup>th</sup> International ERCOFTAC Symposium on Engineering Turbulence Modelling and Measurements, Marseille (France) 9-11 June 2010, Vol. 3, pp. 905–910
- Forestier N, Jacquin L, Geffroy, P (2003) The mixing layer over a deep cavity at high-subsonic speed. *J Fluid Mech* 475:101–145
- Graftieaux L, Michard M, Grosjean N (2001) Combining PIV, POD and vortex identification algorithms for the study of unsteady turbulent swirling flows. *Meas Sci Technol* 12:1422–1429
- Guermond JL, Migeon C, Pineau G, Quartapelle L (2002) Start-up flows in a three-dimensional rectangular driven cavity of aspect ratio 1:1:2 at  $Re = 1000$ . *J Fluid Mech* 450:169–199
- Haigermoser C, Scarano F, Onorato M (2009) Investigation of the flow in a circular cavity using stereo and tomographic particle image velocimetry, *Exp Fluids* 46:517–526
- Horn B, Schunck B (1981) Determining optical flow. *Artif Intell* 17:185–203
- Kegerise MA, Spina EF, Garg GS, Cattafesta III LN (2004) Mode-switching and nonlinear effects in compressible flow over a cavity. *Phys Fluids* 16(3):678–687
- Knisely C, Rockwell D (1982) Self-sustained low-frequency components in an impinging shear layer, *J Fluid Mech* 116:157–186
- Larchevêque L, Sagaut P, Lê TH, Comte P (2004) Large-eddy simulation of a compressible flow in a three-dimensional open cavity at high Reynolds number. *J Fluid Mech* 516:265–301
- Lawson NJ, Wu J (1999) Three-dimensional particle image velocimetry: a low-cost 35 mm angular stereoscopic system for liquid flows, *Opt Lasers Eng* 32:1–19
- Lecordier B, Trinité M (2003) Advanced PIV algorithms with image distortion - Validation and comparison from synthetic images of turbulent flow, 5<sup>th</sup> International Symposium on Particle Image Velocimetry, Busan (Korea), September 22-24, 2003, Paper 3250
- Lin JC, Rockwell D (2001) Organized oscillations of initially turbulent flow past a cavity. *AIAA J* 39 (6):1139–1151
- Michard M, Favelier T (2004) Développement d'un critère d'identification de structures tourbillonnaires adapté aux mesures de vitesse par PIV, 9<sup>ème</sup> Congrès Francophone de Vélocimétrie Laser, Bruxelles (Belgique), 14-17 septembre 2004
- Migeon C (2000) Contribution à l'analyse de l'écoulement tridimensionnel instable s'établissant à l'intérieur de cavités cylindriques, Ph. D. Thesis, Université de Poitiers
- Migeon C (2002) Details on the start-up development of the Taylor-Görtler-like vortices inside a square-section lid-driven cavity for  $1,000 \leq Re \leq 3,200$ . *Exp Fluids* 33:594–602
- Migeon C, Pineau G, Texier A. (2003) Three-dimensionality development inside standard parallelepipedic lid-driven cavities at  $Re = 1000$ . *J Fluids Structs* 17:717–738
- Nearly MD, Stephanoff KD (1987) Shear-layer-driven transition in a rectangular cavity, *Phys Fluids* 30:2936–2946
- Özsoy E, Rambaud P, Stitou A, Riethmuller ML (2005) Vortex characteristics in laminar cavity flow at very low Mach number, *Exp Fluids* 38:133–145
- Prasad AK (2000) Stereoscopic particle image velocimetry, *Exp Fluids* 29:103–116
- Quénot GM, Pakleza J, Kowalewski TA (1998) Particle image velocimetry with optical flow, *Exp Fluids* 25:177–189
- Quénot GM, Rambert A, Lusseyran F, Gougat P (2001) Simple and accurate PIV camera calibration using a single target image and camera focal length, Fourth International Workshop on Particle Image Velocimetry, paper 1040, Göttingen, Germany, 17-19 September 2001
- Raffel M, Willert CE, Kompenhans J (1998) Particle Image Velocimetry, A Practical Guide, Springer
- Sarohia V (1977) Experimental investigation of oscillations in flows over shallow cavities. *AIAA J* 15:984–991

- Scarano F (2001) Iterative image deformation method in PIV – Review article – Meas Sci Techno 12:1382–1391
- Scarano F, David, L, Bsibsi M, Callaud D (2005) S-PIV comparative assessment: image dewarping+misalignment correction and pinhole+geometric back projection, Exp Fluids, 39:257–266
- Stanislas M, Okamoto K, Kähler CJ, Westerweel J (2005) Main results of the second international PIV challenge, Exp Fluids 39:170–191
- Stanislas M, Okamoto K, Kähler CJ, Westerweel J, Scarano F (2008) Main results of the third international PIV challenge, Exp Fluids 45:27–71
- Westerweel J, Draad AA, Van der Hoeven JGT, Van Oord I (1996) Measurement of fully-developed turbulent pipe flow with digital particle image velocimetry, Exp Fluids 20:165–177